*Acta Oceanol. Sin.*, 2017, Vol. 36, No. 5, P. 73–82
DOI: 10.1007/s13131-017-1005-3
http://www.hyxb.org.cn
E-mail: hyxbe@263.net

# The September 16, 2015 $M_w$ 8.3 Illapel, Chile Earthquake: characteristics of tsunami wave from near-field to far-field

REN Zhiyuan[1], YUAN Ye[1]*, WANG Peitao[1], FAN Tingting[1], WANG Juncheng[1], HOU Jingming[1]

[1] National Marine Environmental Forecasting Center, Beijing 100081, China

Received 6 March 2016; accepted 19 April 2016



**Abstract**

On September 16, 2015, an earthquake with magnitude of $M_w$ 8.3 occurred 46 km offshore from Illapel, Chile, generating a 4.4-m local tsunami measured at Coquimbo. In this study, the characteristics of tsunami are presented by a combination of analysis of observations and numerical simulation based on sources of USGS and NOAA. The records of 16 DART buoys in deep water, ten tidal gauges along coasts of near-field, and ten coastal gauges in the far-field are studied by applying Fourier analyses. The numerical simulation based on nonlinear shallow water equations and nested grids is carried out to provide overall tsunami propagation scenarios, and the results match well with the observations in deep water and but not well in coasts closed to the epicenter. Due to the short distance to the epicenter and the shelf resonance of southern Peru and Chile, the maximum amplitude ranged from 0.1 m to 2 m, except for Coquimbo. In deep water, the maximum amplitude of buoys decayed from 9.8 cm to 0.8 cm, suggesting a centimeter-scale Pacific-wide tsunami, while the governing period was 13–17 min and 32 min. Whereas in the far-field coastal region, the tsunami wave amplified to be around 0.2 m to 0.8 m, mostly as a result of run-up effect and resonance from coast reflection. Although the tsunami was relatively moderate in deep water, it still produced non-negligible tsunami hazards in local region and the coasts of far-field.

**Key words:** 2015 Illapel earthquake, tsunami observation, numerical modeling, far-field, near-field

**Citation:** Ren Zhiyuan, Yuan Ye, Wang Peitao, Fan Tingting, Wang Juncheng, Hou Jingming. 2017. The September 16, 2015 $M_w$ 8.3 Illapel, Chile Earthquake: characteristics of tsunami wave from near-field to far-field. Acta Oceanologica Sinica, 36(5): 73–82, doi: 10.1007/s13131-017-1005-3

## 1 Introduction

On September 16, 2015, an interplate thrust earthquake of $M_w$ 8.3 occurred along subduction zone of Chile, 46 km offshore from Illaple (USGS: 31.6°S, 71.7°W, 22:54:33 UTC). This earthquake event is regarded as the third great earthquake in six years along Chile coast, as the convergent motion of Nazca Plate beneath the South American Plate with a rate of 65–74 mm/a (Kendrick et al., 2001; Demets et al., 2010). As reported by news, a wave of 4.5 m high was observed near the coast of Coquimbo, as well as flooding and inundation in Tongoy and Concón. At least 500 buildings were destroyed in the coast of Tongoy.

The rapid global Centroid-Moment Tensor (gCMT) solution provides the fault parameters with strike (5°), dip (22°), rake (106°), focal depth (17.8 km), and seismic moment $M_0$ is $2.86\times10^{21}$ Nm ($M_w$ 8.2). The initial USGS finite fault solution has provided slightly larger moment of $3.2\times10^{21}$ Nm ($M_w$ 8.3), with a centroid depth of 25 km, strike (4°), and dip (19°). Ye et al. (2016) applied the W-phase inversion method to estimate that the fault parameters ranged from $3.7\times10^{21}$ Nm (dip 16°) to $2.7\times10^{21}$ Nm (dip 22°). One source model proposed by Heidarzadeh et al. (2016) suggested that the large-slip area was 80 km×100 km with an average slip of 5.0 m. The seismic moment of their source reached $4.42\times10^{21}$ Nm ($M_w$ 8.4).

After this tsunami event, NOAA provided the real-time assessment of the 2015 Chile tsunami based on the Short-term Inundation Forecasting for Tsunamis system. The energy of tsunami source based on the inversion of DART measurements was estimated to be $7.9\times10^{13}$ J (Tang et al., 2016). The post-tsunami field survey found that the maximum runup of 13.6 m was recorded in La Cebada (30.97°S, 71.65°W) (Contreras-López et al., 2016). Numerical simulation carried out by Aránguiz et al. (2016) shown that tsunami runup was larger than those of the 2014 Pisagua event, with shorter arrival time.

On April 1, 2014, one similar tsunami generated by the earthquake of $M_w$ 8.2 near Iquique (Chile, 19.610°S, 70.776°W) caused a death toll of at least 7 and 200 injured. The deep-water characteristics of the tsunami were analyzed based on the observations of DART buoys and numerical simulation (Heidarzadeh et al., 2015). They found that it was centimeter-scale tsunami in deep sea, with governing period of 15 min and 21 min. An et al. (2014) attempted to derive the slip distribution by the inversion of the measurements of three DART buoys, while considerable mismatch of up to 10 min in arrival time and 1.0 m in amplitude existed. The local inundation and runup were studied based on field data and numerical modeling (Catalán et al., 2015). In this context, the DART records will be analyzed to describe the character-

Foundation item: The Public Science and Technology Research Funds Projects of Ocean under contract No. 201405026; the National Key Research and Development Program of China under contract No. 2016YFC1401500; the Opening Fund of State Key Laboratory of Ocean Engineering under contract No. 1604.

*Corresponding author, E-mail: yuanye@nmefc.gov.cn

istics of tsunami wave in deep water. Energy decay mechanism of three recent trans-Pacific tsunamis in open ocean was studied by using DART records (Rabinovich et al., 2013). Watada et al. (2014) explained arrival time delays and initial phase reversal were relevant with simulation in the far-field.

In this study, the near-field and deep-water tsunami wave characteristics are investigated based on the analysis of measurements and numerical results, including the arrival time, maximum amplitude distribution, and wave period. A comparison between sources of USGS and NOAA from tsunami modeling perspective is described and discussed. The Pacific-wide distribution of maximum amplitude and decay law of maximum amplitude from near-field to far-field are presented.

## 2 Data and methodology

### 2.1 *Tsunami source*

The USGS solution is used in this study, which gives a focal depth of 25 km, strike angle of 4°, and dip angle of 19°. The events of the geometric size of the September 16, 2015 earthquake are typically about 230 km×100 km (length×width). The rake angle is used as 90°. The slip dislocation is calculated to be 4.64 m. All fault parameters are used to compute the seafloor deformation by Okada model (Okada, 1985), as shown in Fig. 1a. The seafloor deformation ranges from –0.6 m to 1.9 m, with the uplift near the trench axis and subsidence farther in shore. The finite fault model of USGS is made up of 384 unit faults, but the pre-simulation has shown it is not as well as single fault. Here a single fault with uniform slip is adapted for simulation.

The nearest DART 32402 was applied for inversion by Tang et al. (2016), using the measured data of first quarter-, half-, and full-wave, respectively. Five faults were used for inversion, with length of 100 km, width of 50 km. This study will take the inversion results of full-wave. Figure 1b has shown the linear superposition of the seafloor deformation triggered by the five faults. The seafloor deformation ranges from –1.8 m to 2.6 m, which is more concentrated, while source of USGS affects larger area.

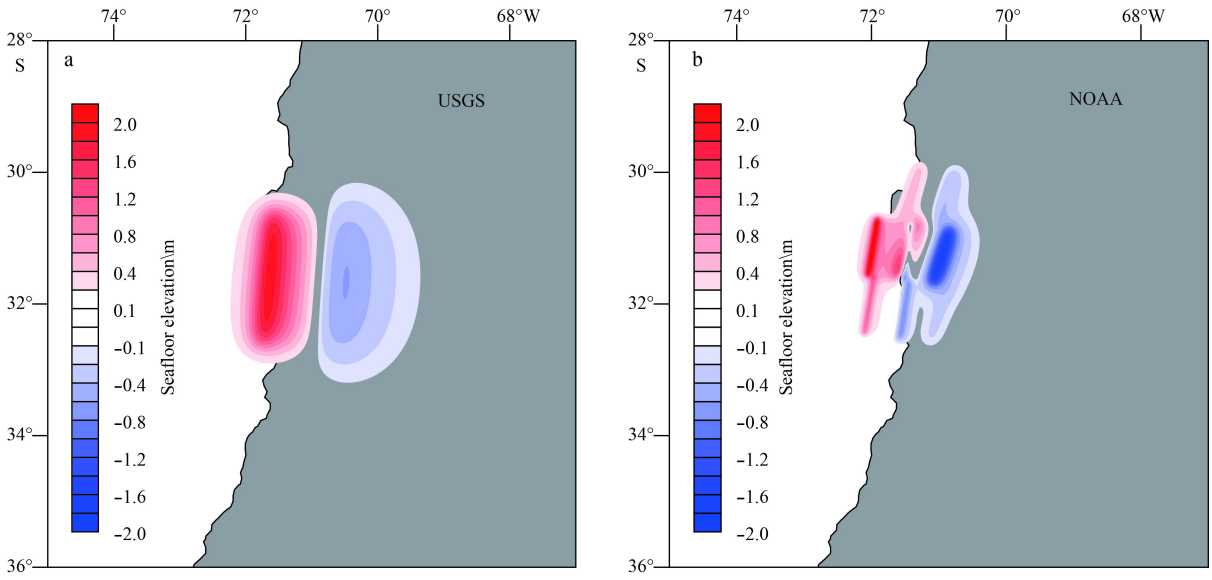


**Fig. 1.** Contours of seafloor deformation.

### 2.2 *Observed data preparation*

The data used in the study includes 16 records of DART buoys provided by the US National Oceanic and Atmospheric Administration (NOAA) and measurements of 26 tidal gauges along coast of South America, as well as ten gauges distributed far-field. The water depth of selected DART buoys is in the range of 3 235–5 848 m, which can display unbiased the characteristics of tsunami propagating in deep water. The distance from the epicenter to the selected buoys ranges from 584 km to 15 868 km.

The original time series of DART data of surface elevation has different sampling intervals of 15 s, 1 min, and 15 min. The buoys can be automatically switched from 15-min model to 15-s model for a few minutes until the termination of the tsunami event (Rabinovich et al., 2013). The interpolation method has been performed to make sure the measured data possesses 1 min sampling interval, and to remove the gaps of time series. Then the band-pass Butterworth filter with cut period of 120 min and 5 min is employed to obtain the tsunami wave. The above processing steps are also applied to time series of tidal gauges to investigate the tsunami wave near coast. The first 3 h of tsunami wave data is extracted for Fourier analysis to study the distribution of power spectrum. As shown in Fig. 2, the yellow circles refer to the DART buoys, while the black dots and red triangles represent the gauges in near-field and far-field.

### 2.3 *Numerical modeling*

Tsunami in the open sea is a kind of shallow water wave, the numerical model GeoClaw is adopted in the study, which is based on the nonlinear shallow water equations and adaptive refined mesh technique (LeVeque et al., 2011). The adaptive refined mesh could help to ensure calculation efficiency, which also can be used for coupled grids. The accuracy of this tsunami model has been verified by simulations of several realistic tsunami events (Ren et al., 2013; Arcos and LeVeque, 2015). It also has been applied in tsunami warning method (Ren et al., 2014), or coupled with Boussinesq model (Ren et al., 2015). The

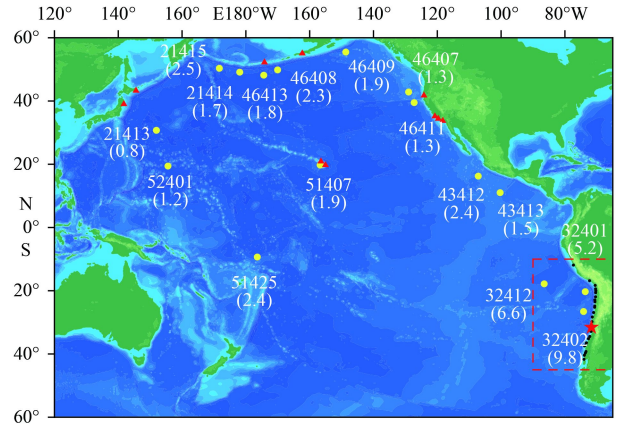


**Fig. 2.** Computational domain and locations of DART buoys and tidal gauges. The red asterisk shows the epicenter. The yellow circles with numbers denote DART buoys, and the maximum amplitudes (cm) are shown in brackets. The tidal gauges in the far-field and near-field are represented by red triangles and black dots respectively. The nested grid is shown with red dash.

basin-wide tsunami simulation is performed within the range of 60°N–60°S, 120°E–65°W. The bathymetry data with 4-min resolution sampled from ETOPO1 is used, and the grid resolution is also 4-min. One nested grid (10°–45°S, 90°–65°W) with 1-min grid and bathymetry data is coupled with the first level grid for tsunami hazard investigation on near-field, which is shown in the red box as shown in Fig. 2. The bathymetry data of 30 s has been used in the region near coastal gauges. The Manning coefficient is 0.024, and the Courant number is set to be 0.75. The simulation results are compared with observations and analyzed in terms of period, arrival time and wave amplitude distribution.

## 3 Impact of the tsunami wave in the near-field

### 3.1 *Wave amplitude distribution*

Figure 3 illustrates the maximum wave amplitude distribution along Chile coast. Figures 3a and b are the simulated maximum wave amplitude distribution in coastal water using source of USGS and NOAA respectively, as well as locations of tidal gauges, while the Fig. 3c shows the comparisons of maximum amplitude at tidal gauges between observation and simulation. In the study

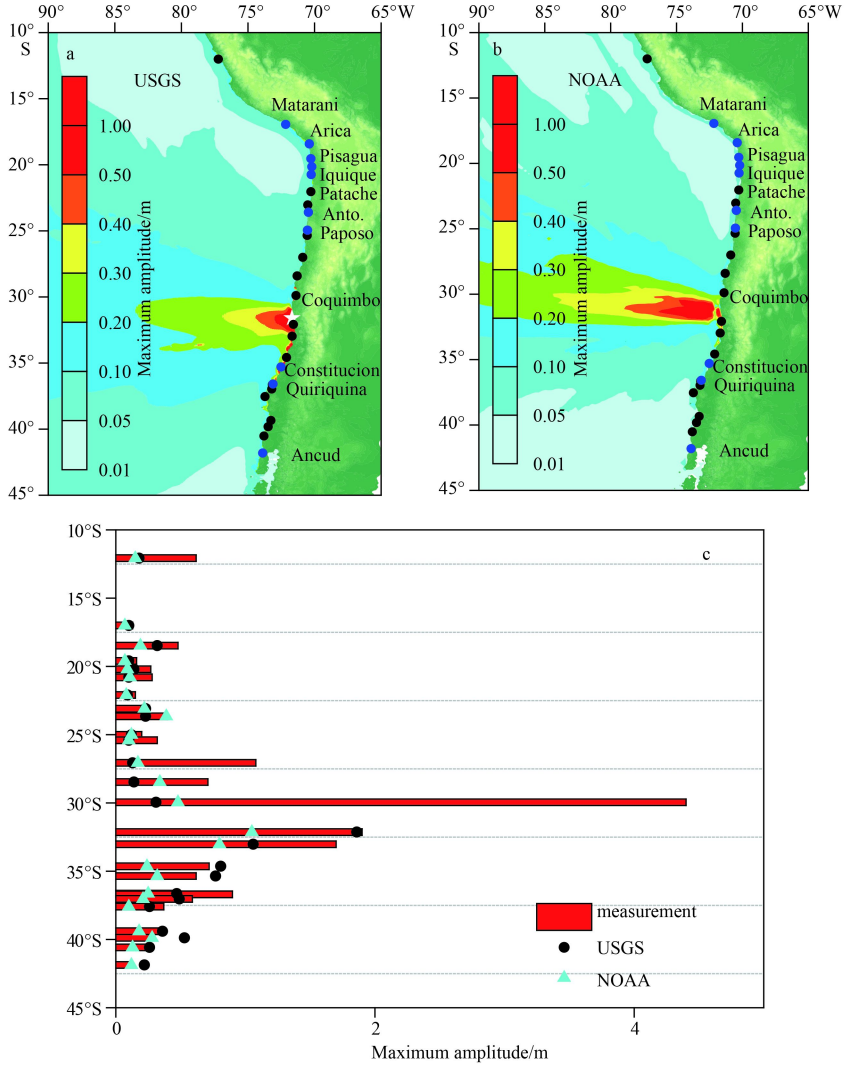


**Fig. 3.** Maximum wave amplitude distribution. a. Simulation results based on USGS source, b. simulation results based on NOAA source, and c. gauges along coast.

of Tang et al. (2016), the modeled the time series of tsunami wave at Coquimbo, Valparaiso matched well with observed data. But the numerical results of this study in regions of 25°–30°S cannot reach measured value, due to insufficient topography data. From Peru coast to South Chile, the tsunami waves exhibit considerable variability, with local maximum amplitude reaching up to 4.4 m, and falling down to 0.1 m. The main effect concentrated in the range of several hundred kilometers near the epicenter. The orientation of tsunami energy beam was towards the Pacific Ocean, and produced tsunami wave more than 0.2 m within a large area. The maximum amplitude along coast was 4.4 m at Coquimbo, and three neighboring gauges (Caldera, Pichidangui, and Valparaiso) received tsunami wave more than 1 m. The distance from the epicenter is 187, 511, 62, 159 km, respectively. It indicates the most hazardous zone is not the closest area to the epicenter, which may be influenced by the complexity of slip distribution, source geometry, and local topography. As stated by Contreras-López et al. (2016), the bay or semi-closed basin in the coastal region can amplify the tsunami wave. The amplitude of other gauges ranged from 0.1 to 0.9 m.

### 3.2 *Waveforms properties and tsunami propagation scenarios*

As shown in Fig. 4, simulated tsunami waves from sources of USGS and NOAA at tidal gauges along the Chile coast are compared with observations, the companion boxes present the power spectras of the corresponding sea level fluctuation. Generally, the numerical results match well with the measured data in most locates, in terms of the leading wave and two or three following tail

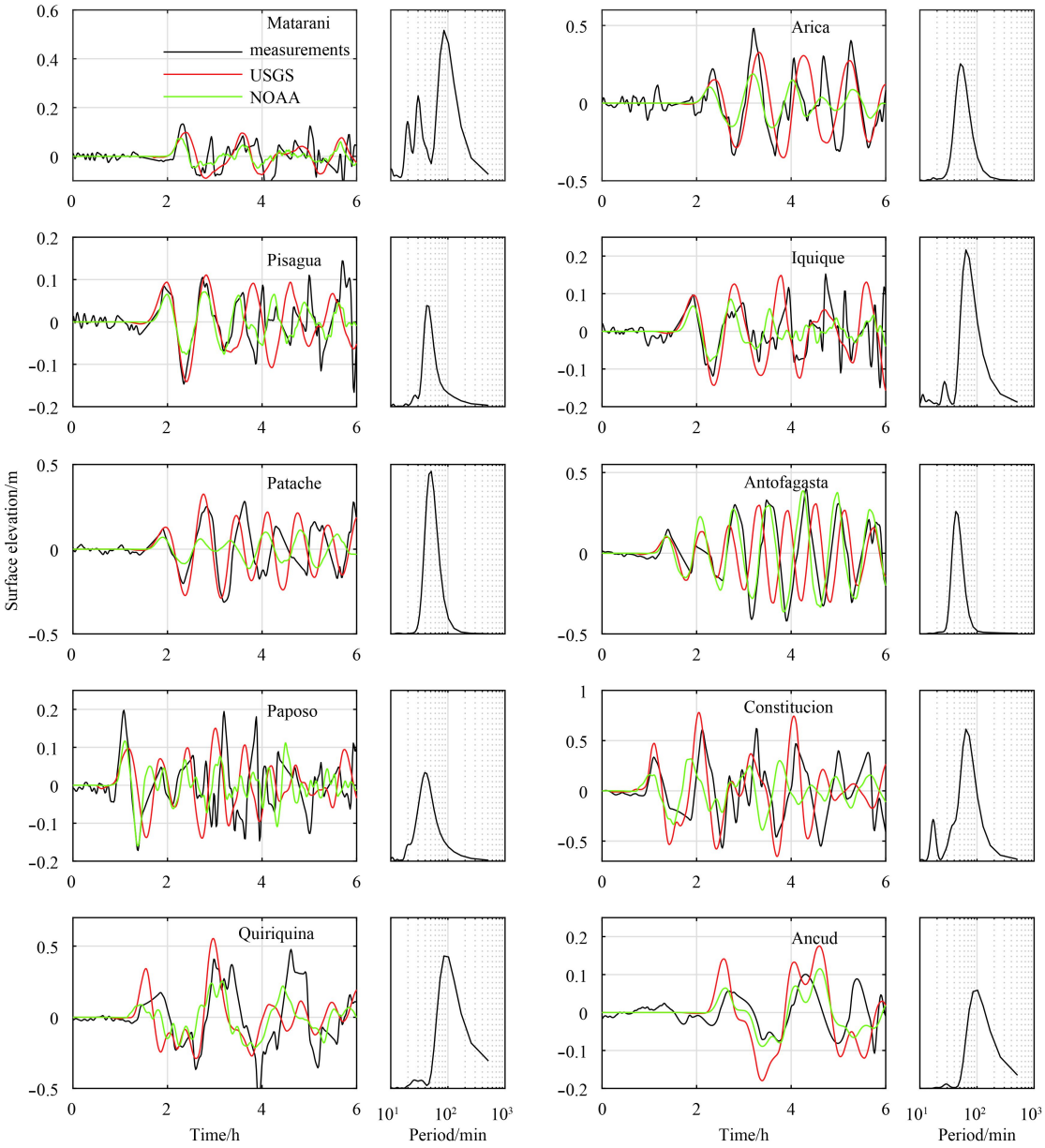


**Fig. 4.** Comparisons of time series of surface elevation with tidal gauges along coast of South America, along with respective spectra. The black line represents the measurements, while red and green lines indicate the numerical results induced by source of USGS and NOAA respectively. The gauge names are included in the figures. The value of vertical axes for the frequency spectra plots are omitted for the reason that we do not focus on the amount of spectral energy in this study.

waves. At Arica, Iquique, Patache, and Constitucion, USGS source can produce better numerical results than NOAA source, while the situation is opposite for Antofagasta and Ancud. Due to the affecting of the complex topography near coast and reflecting wave, the period had shown variability for relatively remote stations. The wave period ranged from 43 min to 64 min for most gauge stations, except for Mataranl (85 min), Quiriquina (102 min) and Ancud (102 min). At many tidal gauge stations, the maximum amplitude did not appear in the leading wave (Arica, Pisagua, Patache, Antofagasta, etc.), which indicated the resonance of tsunami wave due to the reflection of wave from the coasts.

The scenarios of tsunami propagation triggered by USGS source in near-field from 0.5 h to 4.0 h are plotted in Fig. 5, and time interval is 0.5 h. The tsunami firstly formed in central Chile, then spread towards the Pacific Ocean. The land boundary had reflection effect and produced secondary tsunami wave. The leading wave arrived in Peru in around 2 h.

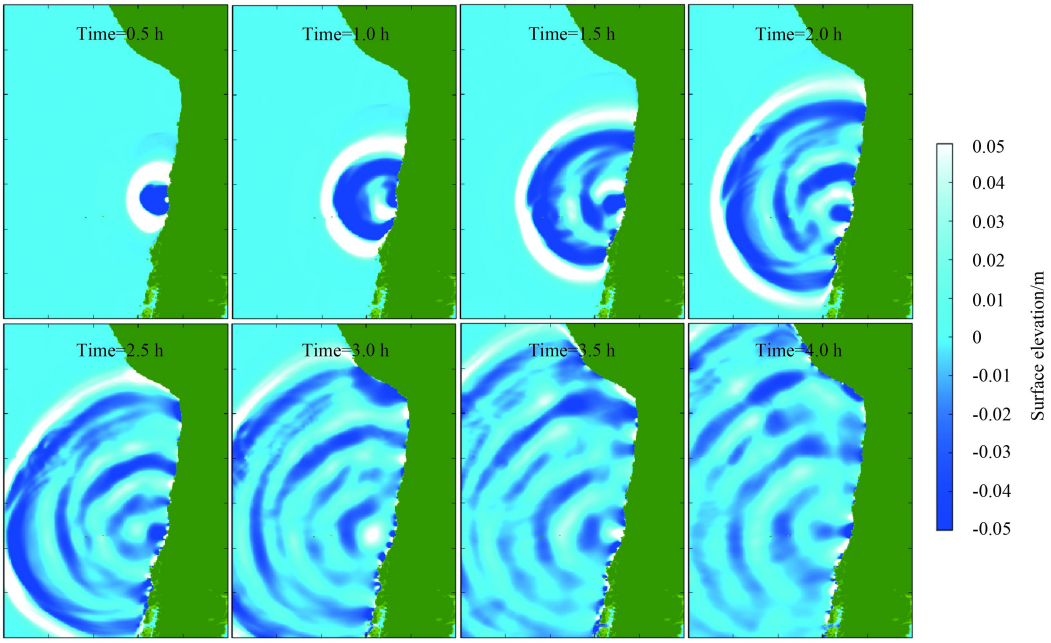


**Fig. 5.** Scenarios of tsunami propagation in near-field based on USGS source in the first 4 h, the time interval is 0.5 h.

## 4 Tsunami wave in the far-field

### 4.1 *Characteristics of trans-Pacific tsunami in deep water*

To better understand the tsunami waveforms and their properties in deep-sea water, the comparisons of time histories of surface elevation between DART buoys' measurements and numerical results from near-field to far-field are presented in Fig. 6, as well as the respective spectras. Generally, the numerical results match well with the measured data at most buoys in terms of the arrival time and maximum amplitude, and NOAA source will reproduce better results than source of USGS for most buoys. The observed tsunami arrival times were delayed by 6–21 min compared with the simulated results for both tsunami sources, with delay time approximately proportional to the discance from the epicenter, which were also reported (Okal, 2011; Rabinovich et al., 2013; Heidarzadeh et al., 2015). The phase reversal of tsunami from the April 1, 2014 $M_w$ 8.2 Iquique, Chile Earthquake was 1-17 min and related to the distance from source (Heidarzadeh et al., 2015).

The parameters of stations and the characteristics of the tsunami waveforms are summarized in Table 1. We do not use the normalized wave height derived by Green's law, as shown in the study of Heidarzadeh et al. (2015). Because the water depth of DART buoys we used here is all deeper than 3 200 m, and it will not make too much differences.

The distance from the epicenter versus travel time and maximum amplitude are plotted in Fig. 7, to explore the decay law of the amplitude and the propagation distance. It was almost the linear relationship between the propagation distance and the tsunami travel time, indicated that the tsunami wave did not represent much nonlinearity due to the deep water depth. The wave speed was approximate to 769 km/h, which average water depth for the tsunami propagation in the Pacific was around 4 659 m. The numerical model reproduces similar maximum amplitude with the observations. The decay law of the maximum amplitude seems like exponential function, and one fitting curve $y$=362.59$x^{-0.574}$ has been added in the figure with black line. It is interesting to find that this decay law is identical with the tsunami observations from the April 1, 2014 $M_w$ 8.2 Iquique, Chile Earthquake. The max amplitude was 23 cm at start (DART 32401), but was reduced to around 0.5–1.0 cm in deep water after propagation for a distance of 8 000 km.

In the near-field, the period of the nearest buoys (DART 32402) was 13, 21, 32, and 64 min, while the most dominant period is 32 min. It was also around 30 min for DART 32412 and 43413. For the middle-field, the spectra was relatively with two major peaks around 17 min and 32 min or 64 min. It turn out that the tsunami wave with different frequency began to separate after some distance of propagation due to dispersion effect. The periods of DART buoys in the far-field performed more complexity, the periods were 13–17 min, 28–34 min, 64 min, even 85 min for the farthest buoys. According to Table 1 and Fig. 6, the domin-

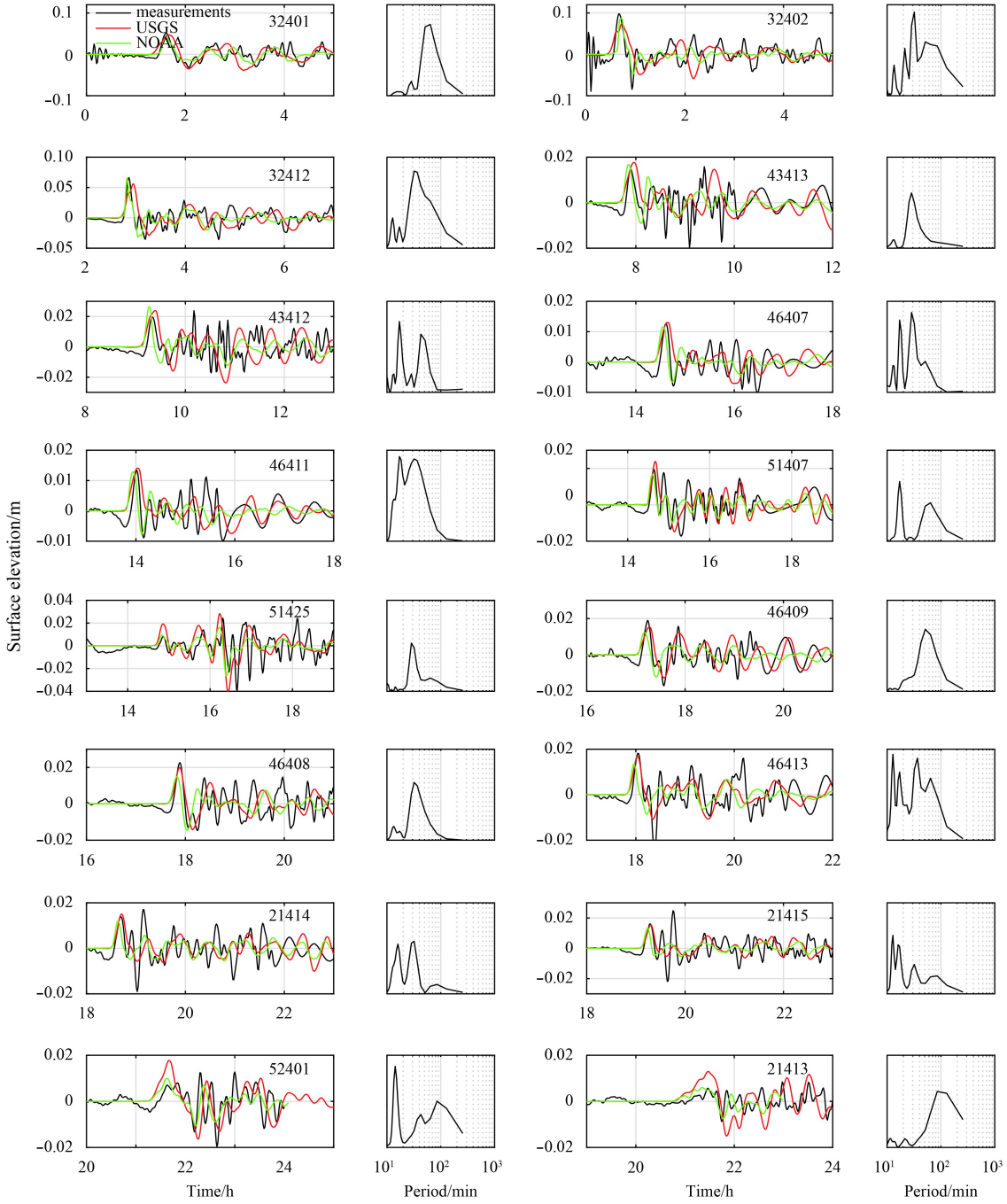


**Fig. 6.** Tsunami wave at DART buoys along with respective spectra. The black line represents the measurements, while red line and green line indicate the numerical results using USGS and NOAA source respectively. The DART number is included in the figures. Time shift for DART buoys are 32401 (–6 min), 32402 (–6 min), 46407 (5 min), 46411 (5 min), 51407 (9 min), 51425 (13 min), 46409 (6 min), 46408 (9 min), 46413 (9 min), 21414 (12 min), 21415 (12 min), 52401 (21 min), and 21413 (15 min).

ant period for the tsunami wave in deep water was 13–17 min, and 32 min.

To estimate the dimensions of tsunami source from the governing period (Heidarzadeh and Satake, 2013), the following equation is used:

$$\lambda = T\sqrt{gh}, \tag{1}$$

where $\lambda$ is wavelength in meters, $g$ is the gravitational acceleration, $T$ is the period of the tsunami wave in seconds, and $h$ is wave depth near the tsunami source in meters. The average depth near the source area is around 4 500 m, the period 15 min and 32 min are applied in Eq. (1) to obtain 202 km and 95 km for the length and width, respectively. It is agree with initial estimation of USGS.

The tsunami propagation scenarios based on USGS source in the Pacific Ocean are described in Fig. 8, the time interval is 2 h. After generating from Chile, the tsunami spread into the Pacific Ocean. It underwent refraction and diffraction near the Tahiti Island in 9 h. Although this tsunami affected the most part of the Pacific Ocean, it had less impact in 23 h, which only generated

**Table 1.** The DART buoys and the characteristics of the tsunami waveforms

| Dart No. | South latitude/(°) | West longitude/(°) | Depth/m | Distance/km | Arrival time/h | A_obs./cm | A_sim./cm | Period/min |
|---|---|---|---|---|---|---|---|---|
| 32402 | –26.74 | –73.98 | 4 070 | 584 | 0.54 | 9.8 | 7.5 | 13, 21, 32, 64 |
| 32401 | –20.47 | –73.43 | 4 797 | 1 245 | 1.41 | 5.2 | 4.6 | 64 |
| 32412 | –17.98 | –86.33 | 4 387 | 2 111 | 2.68 | 6.6 | 5.6 | 13, 32 |
| 43413 | 10.84 | –100.14 | 3 560 | 5 607 | 7.76 | 1.5 | 1.8 | 28 |
| 43412 | 16.07 | –107.00 | 3 200 | 6 502 | 9.14 | 2.4 | 2.4 | 17, 43 |
| 46411 | 39.33 | –127.08 | 4 334 | 9 739 | 13.82 | 1.3 | 1.4 | 17, 32 |
| 46407 | 42.67 | –128.81 | 3 323 | 10 104 | 14.42 | 1.3 | 1.3 | 13, 17, 28 |
| 51407 | 19.59 | –156.55 | 4 738 | 10 669 | 14.41 | 1.9 | 2.4 | 17, 64 |
| 51425 | –9.51 | –176.24 | 4 960 | 10 802 | 14.71 | 2.4 | 2.8 | 28 |
| 46409 | 55.30 | –148.51 | 4 200 | 12 084 | 17.05 | 1.9 | 1.5 | 51 |
| 46408 | 49.67 | –169.89 | 5 412 | 13 183 | 17.69 | 2.3 | 2.0 | 32 |
| 46413 | 48.00 | –174.23 | 5 614 | 13 440 | 17.84 | 1.8 | 1.7 | 13, 17, 37, 64 |
| 21414 | 48.95 | 178.25 | 5 375 | 14 004 | 18.48 | 1.7 | 1.5 | 16, 32 |
| 21415 | 50.18 | 171.85 | 4 745 | 14 477 | 19.06 | 2.5 | 1.5 | 13, 17, 32 |
| 52401 | 19.26 | 155.75 | 5 574 | 15 097 | 20.23 | 1.2 | 1.8 | 14, 85 |
| 21413 | 30.55 | 152.13 | 5 848 | 15 868 | 20.91 | 0.8 | 1.3 | 85 |

Note: A_obs. denotes the observed maximum amplitude and numerical results based on USGS source are indicated by A_sim.

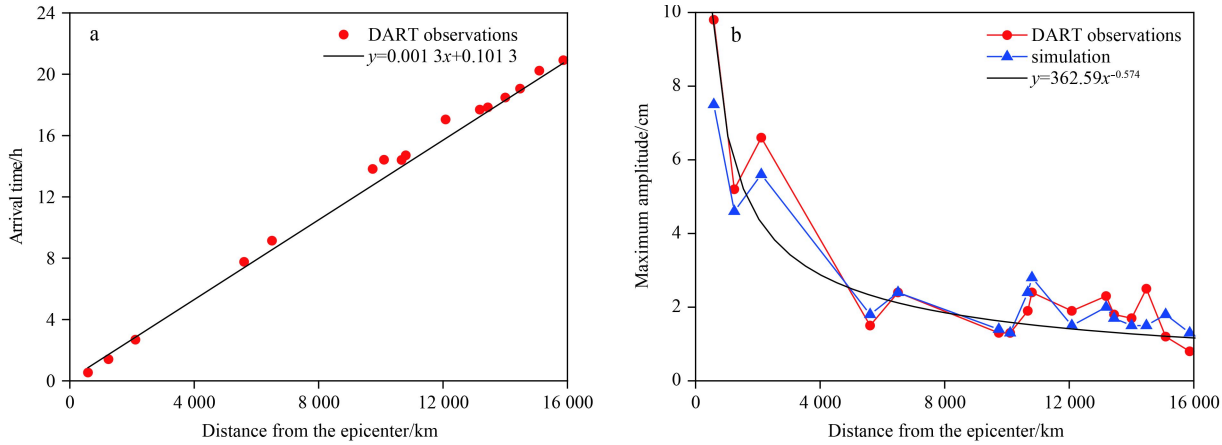


**Fig. 7.** Relationships between the distance from the epicenter and arrival time (a) and maximum amplitude (b). The red dot denotes observations of DART buoys, and the red triangle represents simulation results. Black line indicates the fitting curve $y=362.59x^{-0.574}$ in the right figure.

tsunami wave of 1 cm. Figure 9 presents the contours of maximum amplitude distribution and arrival time, which indicates this relatively moderate tsunami event caused fluctuation of sea water in the region of the Pacific Ocean.

### 4.2 *Characteristics of tsunami wave at coastal regions of far-field*

To evaluate the tsunami's impacts on the coasts in the far-field, measurements from ten tidal gauges in California (Los Angeles, Santa Barbara, Crescent City, and Port San Luis), Hawaii (Hilo and Kahului), Alaska (King Cove and Atka), and Japan (Hanasaki and Ofunato) are selected to analyze, as shown in Fig. 10. Due to lack of high-resolution topography data, only observations are analyzed here. Although the tsunami only induces 9.8-centermeter wave in deep sea of near-field (DART 32402), the tsunami produced larger tsunami wave at the coasts of far-field. It is noted that California received tsunami wave of around 0.2 m amplitude, nearly 0.8 m tsunami in Hawaii, more or less than 0.2 m tsunami in Alaska, and even 0.2 m in Japan.

The tsunami wave period for Los Angeles and Santa Barbara both were 64 min, 51 min for Port San Luis, while 17 and 37 min for Crescent City for the harbor resonance. The governing period for Hawaii at Hilo and Kahului was 17 min and 16 min respectively. The King Cove possessed 14 min period, while Atka's period was 64 min. Due to the gauge location, the periods of Hanasaki and Ofunato were different, 30 min and 14 min.

## 5 Conclusions

In this work, the tsunami generated by the September 16, 2015 $M_w$ 8.3 Illapel (Chile) earthquake is studied by analysis of the measurements of DART buoys in deep water and tidal gauges near coasts, as well as applying numerical simulation based on different tsunami sources. Although the inversion source by NOAA can produce better numerical results than single fault, it is stated that a single fault with uniform slip can be used for the ini-

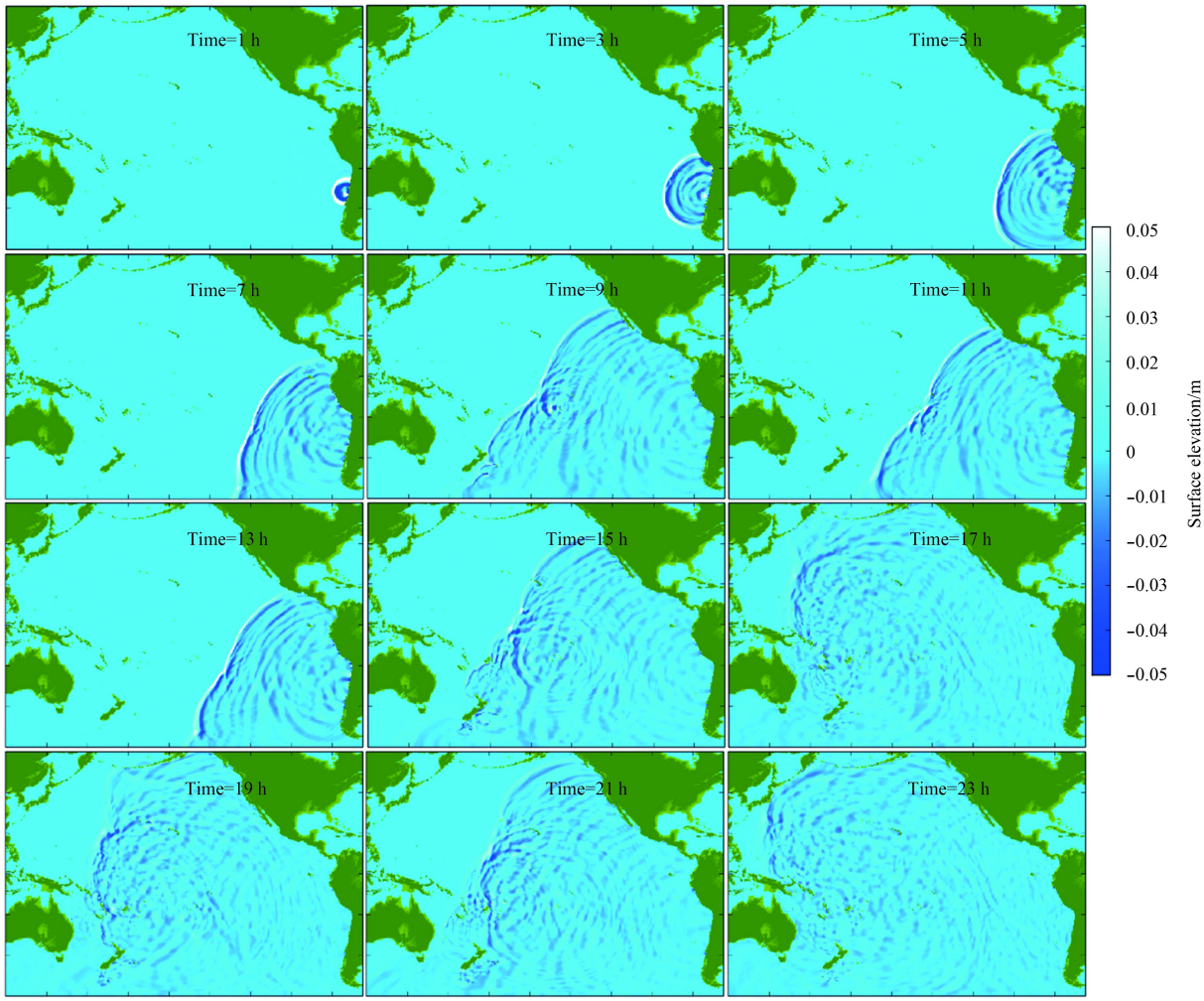


**Fig. 8.** Scenarios of tsunami propagation in the Pacific Ocean based on USGS source, the time interval is 2 h.

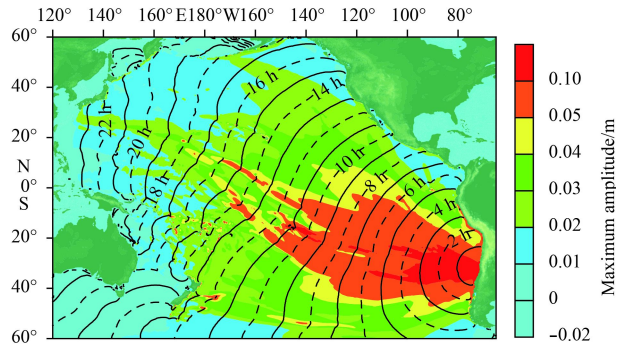


**Fig. 9.** Contours of maximum amplitude distribution and arrival time (USGS source).

tial tsunami hazard investigation. For such medium tsunami waves, the dispersive effects are important, while the nonlinear effects are not significant for deep water. The characteristics of tsunami wave are summarized as followed.

(1) The maximum amplitude in the near-field was 4.4 m at Coquimbo, and the other three gauges received more than 1 m tsunami wave were within the range of around 500 km from the epicenter. Most wave periods along the coast of the near-field were 43–64 min.

(2) It is found that the maximum amplitude in deep water decays from 9.8 cm to 0.8 cm as the tsunami propagated from 584 km to 15 868 km. The decay scale is approximate to exponential decay, corresponding to the tsunami generated by the April 1, 2014 $M_w$ 8.2 Iquique, Chile Earthquake. The governing period was 13–17 min and 32 min.

(3) As the tsunami propagated to the shore even in the far-field, the tsunami amplitude increased to around 0.2–0.8 m from centimeter-scale in deep water, due to run up of tsunami wave and resonance from coast reflection. The period was in a wide range for the influence of topography and long distance propagation.

Considering the impact of the coast, the governing period of the tsunami in deep sea is adopted, which is 13–17 min and 32 min. The tsunami only induced less than 0.2 m tsunami near Japan coast, it is believed this tsunami did not induce any impacts on China coast, while 2010 Chile $M_w$ 8.8 only produced the maximum amplitude of 32 cm in China coast (Yu et al., 2011). The minor effects on China's coastline are due to shielding effects by island chain such as Ryukyu, Penhu, etc. Although this tsunami is relatively moderate, as noted centimeter-scale tsunami in deep water, it still resulted in the damages to coastal infrastructures and some impacts on the coasts in the near-field and far-field. It is suggested that such moderate earthquake tsunami also need to

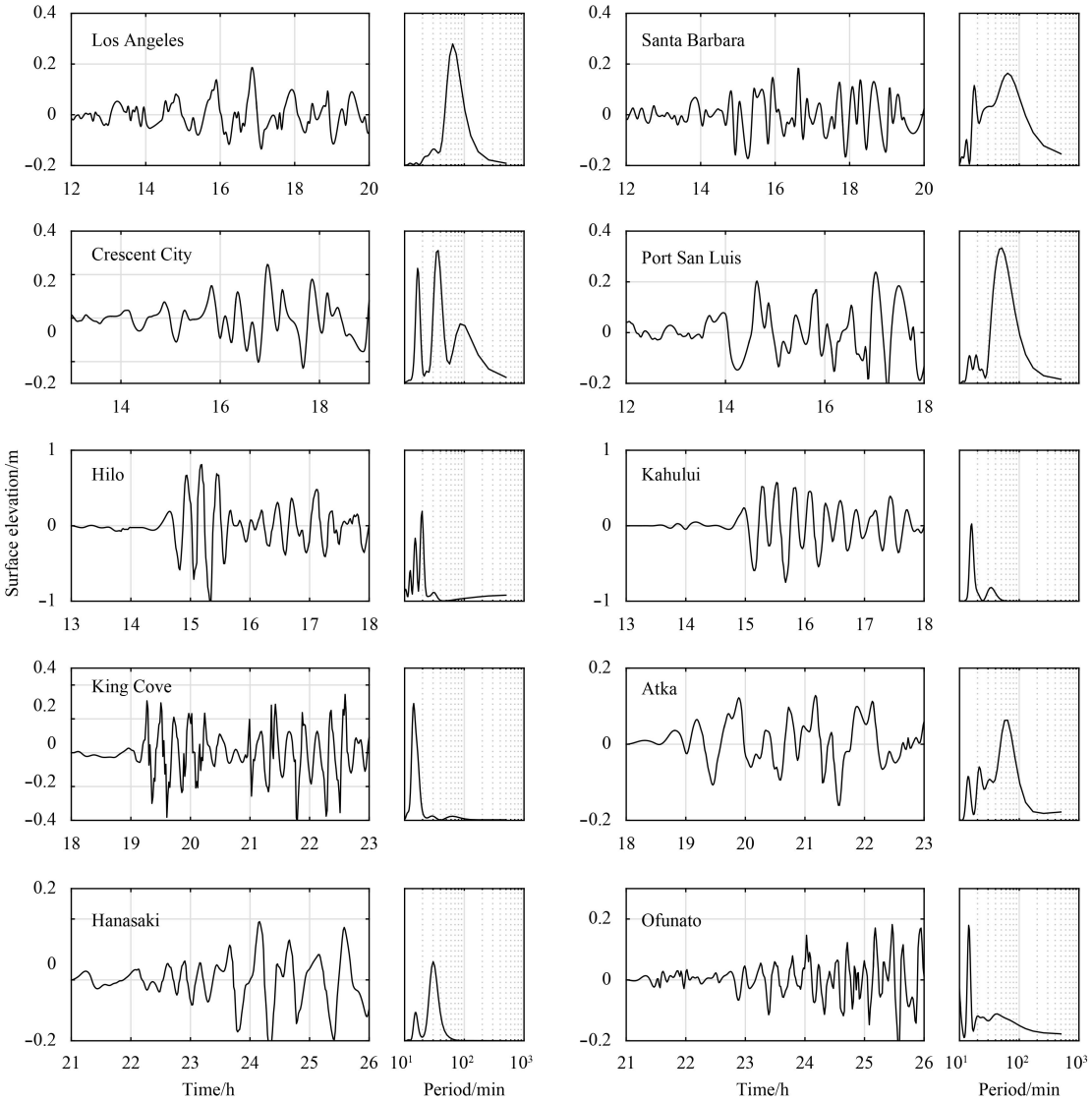


**Fig. 10.** Measured tsunami waveforms and their spectras for the coastal regions of far-field.

pay attention, including tsunami hazard assessment for the regions in near-field and development the tsunami early warning method for the near-field.

***Acknowledgements***

Special thanks to Liu Hua at Shanghai Jiao Tong University and Christopher Earls Brennen at Caltech for their encouragement and suggestion on my research work. The valuable comments from the reviewers enhanced this study.

**References**

An Chao, Sepúlveda I, Liu P L F. 2014. Tsunami source and its validation of the 2014 Iquique, Chile, earthquake. Geophysical Research Letters, 41(11): 3988–3994

Aránguiz R, González G, González J, et al. 2016. The 16 September 2015 Chile Tsunami from the post-tsunami survey and numerical modeling perspectives. Pure and Applied Geophysics, 173(2): 333–348

Arcos M E M, LeVeque R J. 2015. Validating velocities in the GeoClaw tsunami model using observations near Hawaii from the 2011 Tohoku tsunami. Pure and Applied Geophysics, 172(3–4): 849–867

Catalán P A, Aránguiz R, González G, et al. 2015. The 1 April, 2014 Pisagua tsunami: observations and modeling. Geophysical Research Letters, 42(8): 2918–2925

Contreras-López M, Winckler P, Sepúlveda I, et al. 2016. Field survey of the 2015 Chile Tsunami with emphasis on coastal wetland and conservation areas. Pure and Applied Geophysics, 173(2): 349–367

DeMets C, Gordon R G, Argus D F. 2010. Geologically current plate motions. Geophysical Journal International, 181(1): 1–80

Heidarzadeh M, Satake K. 2013. Waveform and spectral analyses of the 2011 Japan tsunami records on tide gauge and DART stations across the Pacific Ocean. Pure and Applied Geophysics, 170(6–8): 1275–1293

Heidarzadeh M, Murotani S, Satake K, et al. 2016. Source model of the 16 September 2015 Illapel, Chile, $M_w$ 8.4 earthquake based on teleseismic and tsunami data. Geophysical Research Letters, 43(2): 643–650

Heidarzadeh M, Satake K, Murotani S, et al. 2015. Deep-water characteristics of the trans-Pacific tsunami from the 1 April 2014 $M_w$ 8.2 Iquique, Chile Earthquake. Pure and Applied Geophysics, 172(3–4): 719–730

Kendrick E, Bevis M, Smalley Jr R, et al. 2001. An integrated crustal velocity field for the central Andes. Geochemistry, Geophysics, Geosystems, 2(11): doi: 10.1029/2001GC000191

LeVeque R J, George D L, Berger M J. 2011. Tsunami modelling with adaptively refined finite volume methods. Acta Numerica, 20: 211–289

Okada Y. 1985. Surface deformation due to shear and tensile faults in a half-space. Bulletin of the Seismological Society of America, 75(4): 1135–1154

Okal E A. 2011. Tsunamigenic earthquakes: past and present milestones. Pure and Applied Geophysics, 168(6–7): 969–995

Rabinovich A B, Candella R N, Thomson R E. 2013. The open ocean energy decay of three recent trans-Pacific tsunamis. Geophysical Research Letters, 40(12): 3157–3162

Ren Zhiyuan, Liu Hua, Wang Benlong, et al. 2014. An investigation on multi-buoy inversion method for tsunami warning system in South China Sea. Journal of Earthquake and Tsunami, 8(3): 1440004

Ren Zhiyuan, Wang Benlong, Fan Tingting, et al. 2013. Numerical analysis of impacts of 2011 Japan Tohoku tsunami on China Coast. Journal of Hydrodynamics, Serise B, 25(4): 580–590

Ren Zhiyuan, Zhao Xi, Liu Hua. 2015. Dispersion effects on tsunami propagation in South China Sea. Journal of Earthquake and Tsunami, 9(5): 1540001

Tang Liujuan, Titov V V, Moore C, et al. 2016. Real-time assessment of the 16 September 2015 Chile Tsunami and implications for near-field forecast. Pure and Applied Geophysics, 173(2): 369–387

Watada S, Kusumoto S, Satake K. 2014. Traveltime delay and initial phase reversal of distant tsunamis coupled with the self-gravitating elastic Earth. Journal of Geophysical Research: Solid Earth, 119(5): 4287–4310

Ye Lingling, Lay T, Kanamori H, et al. 2016. Rapidly estimated seismic source parameters for the 16 September 2015 Illapel, Chile $M_w$ 8.3 Earthquake. Pure and Applied Geophysics, 173(2): 321–332

Yu Fujiang, Yuan Ye, Zhao Lianda, et al. 2011. Evaluation of potential hazards from teletsunami in China: tidal observations of a teletsunami generated by the Chile 8.8 $M_w$ earthquake. Chinese Science Bulletin, 56(11): 1108–1116